

Comparison of the Tidal Signatures in Sporadic E and Vertical Ion Convergence Rate, Using FORMASAT-3/COSMIC Radio Occultation Observations and GAIA Model

Sahar Sobhkhiz-Miandehi (✉ sobhkhizsahar@yahoo.com)

gfz german research centre for geosciences <https://orcid.org/0000-0002-8668-9042>

Yosuke Yamazaki

GFZ: Deutsches Geoforschungszentrum Potsdam

Christina Arras

GFZ: Deutsches Geoforschungszentrum Potsdam

Yasunobu Miyoshi

Kyushu University

Hiroyuki Shinagawa

national institute of information and communication technology

Full paper

Keywords: Sporadic E, Es, wind shear, solar tide, lunar tide, GAIA, radio occultation

Posted Date: November 10th, 2021

DOI: <https://doi.org/10.21203/rs.3.rs-1029914/v1>

License:   This work is licensed under a Creative Commons Attribution 4.0 International License.

[Read Full License](#)

1 **Title: Comparison of the Tidal Signatures in Sporadic E and Vertical Ion**
2 **Convergence Rate, Using FORMASAT-3/COSMIC Radio Occultation Observations**
3 **and GAIA Model**

4 Author#1: Sahar Sobhkhiz-Miandehi, GFZ German Research Centre for Geosciences-
5 Potsdam-Germany, & Faculty of Science-University of Potsdam- Potsdam- Germany,
6 sahar@gfz-potsdam.de

7 Author#2: Yosuke Yamazaki, GFZ German Research Centre for Geosciences- Potsdam-
8 Germany, yamazaki@gfz-potsdam.de

9 Author#3: Christina Arras, GFZ German Research Centre for Geosciences-Potsdam-
10 Germany, arras@gfz-potsdam.de

11 Author#4: Yasunobu Miyoshi Kyushu University-Fukuoka-Japan,
12 miyoshi.yasunobu.527@m.kyushu-u.ac.jp

13 Author#5: Hiroyuki Shinagawa, National Institute of Information and Communications
14 Technology-Tokyo-Japan, sinagawa@nict.go.jp

15 **Corresponding author: Sahar Sobhkhiz-Miandehi**

16 **Abstract**

17 Sporadic E or Es is a transient phenomenon where thin layers of enhanced electron
18 density appear in the ionospheric E region (90-120 km altitude). The neutral wind shear
19 caused by atmospheric tides can lead ions to converge vertically at E-region heights and
20 form the Es layers. This research aims to determine the role of atmospheric solar and
21 lunar tides in Es occurrence. For this purpose, radio occultation data of FORMASAT-
22 3/COSMIC have been used, which provides complete global coverage of Es events.
23 Moreover, GAIA model simulations have been employed to evaluate the vertical ion
24 convergence induced by solar tides. The results show both migrating and non-migrating
25 solar tidal signatures and the semidiurnal migrating lunar tidal signature in Es occurrence.
26 The seasonal variation of the migrating solar tidal components of Es is in good agreement
27 with those in the vertical ion convergence derived from GAIA. Furthermore, some non-
28 migrating components of solar tides, including semidiurnal westward wavenumbers 1 and
29 3 and diurnal eastward wavenumbers 2 and 3, also significantly affect the Es occurrence
30 rate.

31 **Keywords**

32 Sporadic E, Es, wind shear, solar tide, lunar tide, GAIA, radio occultation

33 **Introduction**

34 Thin layers of enhanced electron density, which are detected in the lower thermosphere
35 at the altitude range of 90 to 120km, are referred to as Sporadic E and abbreviated as Es
36 (Haldoupis, 2011; Mathews, 1998; Whitehead, 1989). This transient phenomenon
37 frequently occurs at mid and low latitudes (Christakis et al., 2009; Haldoupis, 2012;
38 Haldoupis et al., 2007), mainly during the daytime in the summer hemisphere (Arras et
39 al., 2010). Es layers have been the subject of many studies since the mid-twentieth century
40 (e.g., Macleod, 1966; Whitehead, 1961, 1970, 1989) due to their impact on radio wave
41 propagation in communication and navigation systems.

42 Wind shear theory is the most commonly accepted physical mechanism for midlatitude
43 Es layer formation (Haldoupis & Pancheva, 2002; Haldoupis, 2011). According to wind
44 shear theory, metallic ions such as Fe^+ , Na^+ , and Ca^+ in the ionosphere dynamo region,
45 influenced by vertical shears of horizontal wind and the Earth's magnetic field, will
46 converge vertically to a thin layer of ionization (Axford & Cunnold, 1966; Haldoupis,

47 2011).

48 The wind shears in the lower thermosphere are mainly produced by atmospheric tides,
49 including solar /lunar tides with the period of a solar /lunar day and its harmonics. Solar
50 tides are known to be the primary source of vertical shears in the neutral wind (Haldoupis,
51 2012); hence a solar tidal signature is expected to be seen in the Es occurrence. Numerous
52 studies have focused on the solar tidal signature in the Es layer. For example, Mathews
53 & Bekey (1979) demonstrated that the vertical motion of Es layers is consistent with
54 diurnal and semidiurnal tides in the neutral atmosphere. Arras et al. (2009) presented
55 semidiurnal solar tidal signatures in Es occurrence rate (EsOR) at northern hemisphere
56 midlatitude (50°-55°N). They compared EsOR with meteor radar wind measurements and
57 found a strong relationship between semidiurnal tides in EsOR and vertical shear of zonal
58 wind. Christakis et al. (2009) studied the midlatitude Es layer seasonal variation and
59 indicated diurnal tide influence on Es at altitudes below 110km and semidiurnal tide
60 dominance above that altitude. Oikonomou et al. (2014) also showed that a semidiurnal
61 tide-like periodicity dominates Es layers. Terdiurnal and quarterdiurnal tidal signatures in
62 Es occurrence rate are also indicated in other publications (e.g., Haldoupis & Pancheva,

63 2006; Fyterer et al., 2013; Jacobi et al., 2019). Recently, Liu et al. (2021) revealed a
64 wavenumber 4 pattern in Es occurrence rate at mid and low latitudes formed by eastward
65 propagating non-migrating diurnal tide with zonal wavenumber 3, and a similar feature
66 was detected in the vertical shear of the zonal wind.

67 Shinagawa et al. (2017) calculated the vertical ion convergence rate using GAIA
68 (Ground-to-topside model of Atmosphere and Ionosphere for Aeronomy) simulations to
69 show how the geographical and seasonal variations of wind shears are consistent with
70 those in EsOR. Some previous studies have utilized GPS radio occultation (RO)
71 measurements and combined them with winds from different models such as HWM07
72 (Horizontal Wind Model 2007), WACCM (the Whole Atmosphere Community Climate
73 Model), and GAIA, to show neutral wind shear correspondence with Es (e.g., Chu et al.,
74 2014; Liu et al., 2018; Qiu et al., 2019; Yeh et al., 2014). However, it is not yet fully
75 understood precisely which components of tides contribute to Es layer formation. This
76 paper provides a tidal spectrum of Es occurrence rate using GPS radio occultation
77 measurements and then compares them with tidal spectra of vertical ion convergence rate
78 using GAIA model simulations.

79 Some investigations have been done on the lunar tide influences on Es using ground-
80 based observations (e.g., Matsushita, 1952, 1957, 1967; Stening, 1999; Tarpley &
81 Matsushita, 1971, 1972), but none of them have provided a global picture of lunar tidal
82 signature in the Es occurrence. The present study will look over global lunar tidal
83 variations of Es occurrence using GPS radio occultation measurements.

84 Apart from atmospheric tides, planetary waves can also contribute to wind shear
85 formation in the lower thermosphere. Some studies have suggested planetary wave effects
86 on Es events (e.g., Haldoupis & Pancheva, 2002; Pancheva et al., 2003; Haldoupis et al.,
87 2004; Voiculescu et al., 1999), but planetary waves are not in the scope of the current
88 paper. Interested readers can refer to the articles mentioned above.

89 **FORMOSAT-3/COSMIC radio occultation data**

90 For many years, Es events were mainly observed by ionosonde and sometimes in situ
91 techniques (Mathews, 1998; Matsushita, 1962; Whitehead, 1989). In the past two decades,
92 many studies have benefited from the new GPS radio occultation methodology to obtain
93 the global distribution of Es layers (Arras et al., 2008; Hocke et al., 2001; Wu et al., 2005).
94 GPS radio occultation is a satellite remote sensing technique in which GPS signals are

95 received by a low earth-orbiting satellite (LEO) after traveling through the atmosphere.
96 Due to the atmospheric refractive index, the signals are bent on their way. This bending
97 angle is the key observation to obtain information of the ionosphere and neutral
98 atmosphere (Arras, 2010).

99 FORMOSAT-3/COSMIC (FORMOSA SATellite mission-3 / Constellation Observing
100 System for Meteorology, Ionosphere and Climate) consists of six LEO satellites, launched
101 on April 2006. At the altitude of 80 to 130km, scintillations are observed in SNR and
102 phase measurements of FORMOSAT-3/COSMIC radio occultation signals, usually
103 caused by Es layers. Signal phase differences, ionospheric excess phase, and SNR values
104 are used in different literature to extract Es events from GPS-RO measurements (Hocke
105 et al., 2001; Wu et al., 2005). EsOR in this study is derived from the signal-to-noise ratio
106 (SNR) profiles of GPS L1 signal of the level 1b atmPhs data product. Limiting thresholds
107 has been set empirically to SNR values, and Es is defined as scintillations with SNR
108 standard deviation more than 0.2 in a narrow altitude range. The method details can be
109 found in Arras & Wickert (2018). Our investigations are based on FORMOSAT-
110 3/COSMIC radio occultation data of the years 2007 to 2017.

111 **GAIA model simulation data analysis**

112 GAIA is a whole atmosphere model that has been developed by coupling three existing
113 models: A whole atmosphere general circulation model (GCM) for deriving atmospheric
114 neutral density, velocity, and temperature; an ionospheric model for ion density, ion, and
115 electron temperature, and electric conductivity; and an electrodynamics model for the
116 electric field (Jin et al., 2011). In the present study, the temperature and composition of
117 the neutral atmosphere and the neutral wind velocity are obtained from the GAIA model
118 with a grid spacing of 2.8° longitude by 2.8° latitude, 0.2 scale height, and a time
119 resolution of 1 hour. We have analyzed GAIA simulation data for the years 2007 to 2017.
120 Neglecting diffusion, electric field force, and vertical component of neutral wind velocity,
121 the vertical ion drift velocity w_i can be written as follows (Mathews, 1998):

122
$$w_i = \frac{r \cos I}{1+r^2} U + \frac{\cos I \sin I}{1+r^2} V \quad (1)$$

123 where I is the Earth's magnetic field dip angle, U and V are magnetic eastward and
124 southward neutral wind velocity, and r is the ratio of the ion-neutral collision frequency
125 to the ion gyrofrequency. In the lower E region (90-115km altitude), $r \gg 1$ (Richmond,
126 1995). Therefore, the zonal wind component is more efficient than the meridional wind

127 component in causing vertical ion motion and, as a result, the Es layer formation

128 (Haldoupis, 2012).

129 Using geographical neutral wind velocities, U and V used in equation (1) are expressed

130 as follows (Qiu et al., 2019):

131
$$\begin{cases} U = U' \cos D - V' \sin D \\ V = V' \cos D + U' \sin D \end{cases} \quad (2)$$

132 where U' and V' are zonal and meridional wind velocities, respectively. U' and V' are

133 derived from the GAIA model, and D is the Earth's magnetic field declination angle,

134 derived from International Geomagnetic Reference Field (IGRF; Finlay et al., 2010). We

135 calculate the average vertical ion convergence rate (VIC) and assume only positive VICs

136 lead to Es layer formation. Therefore, we can write VIC as (Shinagawa et al., 2017):

137
$$\text{VIC} = \begin{cases} -\frac{\partial w_i}{\partial z}, & -\frac{\partial w_i}{\partial z} > 0 \\ 0, & -\frac{\partial w_i}{\partial z} < 0 \end{cases} \quad (3)$$

138 **Results**

139 **Es occurrence rate analysis**

140 The Es occurrence rate is maximum in midlatitude summer hemispheres (Arras et al.,

141 2008), and in the latitude range of 40° to 60° south and north, tidal signatures are clearly

142 seen. Therefore, we have analyzed two local summer periods of FORMOSAT-3/COSMIC

143 radio occultation data: one is for the period of June, July, and August of years 2007 to
 144 2017 at the latitude range of 40° to 60° north, and the other is December, January, and
 145 February of years 2007 to 2017 at the latitude range of 40° to 60° south. Binning the
 146 data into 1km altitude by 1-hour local time grids, altitude-local time cross-sections of the
 147 EsOR for the northern hemisphere summer is presented in Figure 1. Maximum values of
 148 EsOR reach up to 13% in northern hemisphere summer.

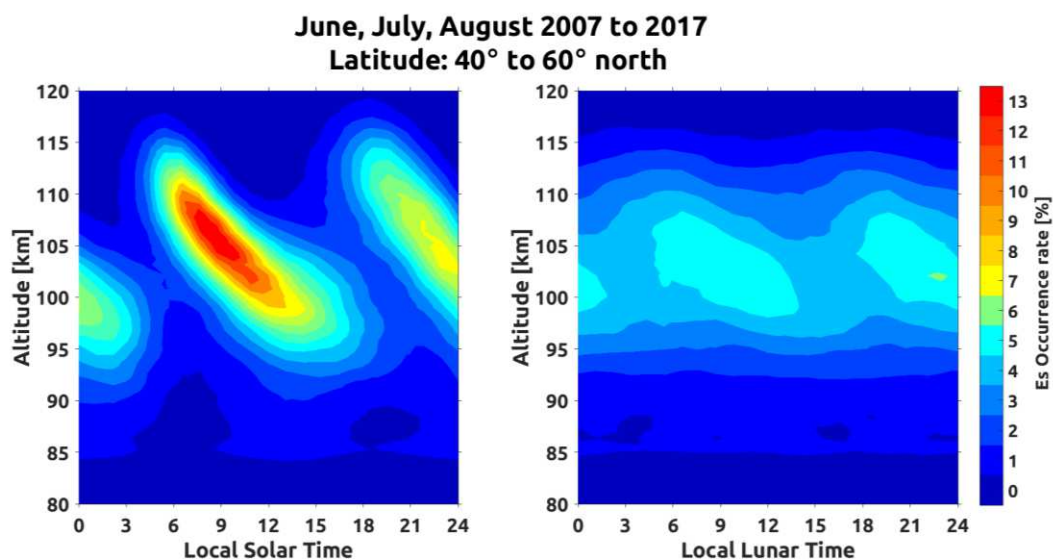


Figure 1 Mid-latitude EsOR variations during northern hemisphere summer with solar local time (left) and lunar local time(right) at different altitudes

149 A descending structure of EsOR with local solar time (LST) and local lunar time (LLT)
 150 is visible. EsOR variations with LST and LLT reveal a semidiurnal pattern at about 95-
 151 115 km altitude. The same applies to southern hemisphere summer shown in Figure 2.
 152 However, the maximum values of EsOR reach only 6.5% in the southern hemisphere,

153 which is almost half of that in the northern hemisphere.

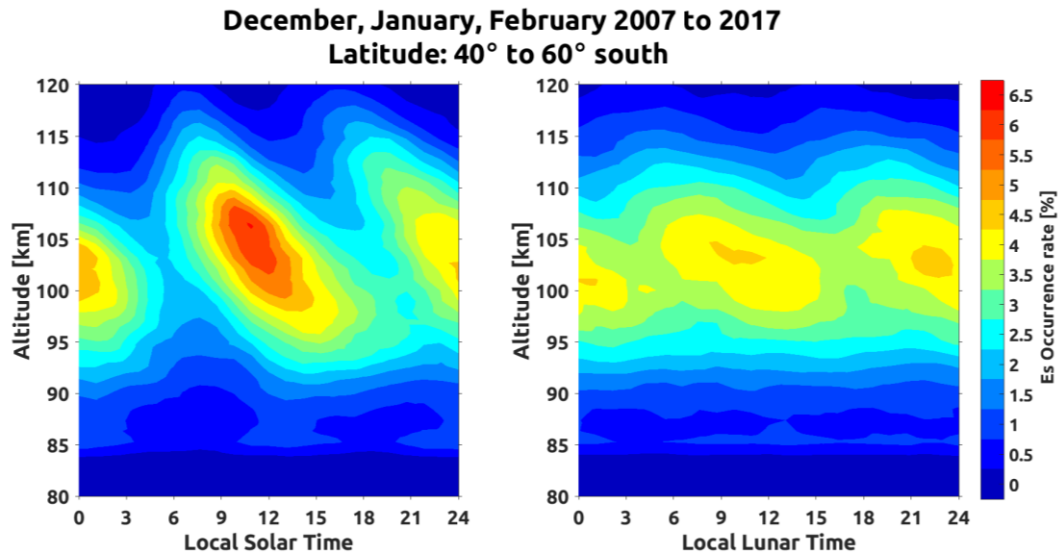


Figure 2 Mid-latitude EsOR variations during southern hemisphere summer with solar local time (left) and lunar local time(right) at different altitudes

154 Tidal modulations at periods of 12 hours are identified in the EsOR, with the peaks around

155 9 and 21 local time in the northern hemisphere. This confirms previous studies on solar

156 and lunar tidal signature detection in northern hemisphere Es layers (e.g., Matsushita,

157 1962; Arras et al., 2009). The phase of solar and lunar tidal signatures are slightly shifted

158 in southern hemisphere EsOR.

159 Spatio-temporal characteristics of EsOR can be quantified using the least-square fitting

160 method. This method estimates the amplitude and phase of tides at a specific frequency

161 and zonal wavenumber, which enables us to separate migrating and non-migrating tidal

162 components. We map the data in the frequency-wavenumber domain, and EsOR

163 measurements can be expressed as:

164
$$EsOR = \sum_{n,s}\{A(n, s) \cos[2\pi(nt + s\lambda)] + B(n, s) \sin[2\pi(nt + s\lambda)]\} \quad (4)$$

165 where n is frequency, s is the wavenumber, t is the normalized time of the day, and λ is

166 the normalized longitude (Lühr & Manoj, 2013). In order to examine tidal components in

167 EsOR, we have limited the data to the altitude range of 95-115km, in which the solar and

168 lunar tidal signatures are dominant and binned them in 10° longitude by 1-hour local

169 time grids. Afterward, frequency-wavenumber analyses have been performed on the data

170 similar to the method suggested in Lühr & Manoj (2013). Tides with the periods of 24h,

171 12h, 8h, 6h respectively are represented by $n=1, 2, 3, 4$ and are referred to as diurnal,

172 semidiurnal, terdiurnal, and quarterdiurnal tides (Forbes et al., 2008).

173 To describe different tidal components, we use the following terminology: tidal periods

174 are represented by D, S, T, and Q, which are respectively corresponding to diurnal,

175 semidiurnal, terdiurnal, and quarterdiurnal tides. Eastward ($s<0$) and westward ($s>0$)

176 propagating tides are represented by E and W. These two letters are followed by an integer

177 representing the zonal wavenumber. For example, DW1 means diurnal westward

178 wavenumber1, SE2 means semidiurnal eastward wavenumber 2, etc. The standing
 179 components are denoted as D0, S0, T0, and Q0.

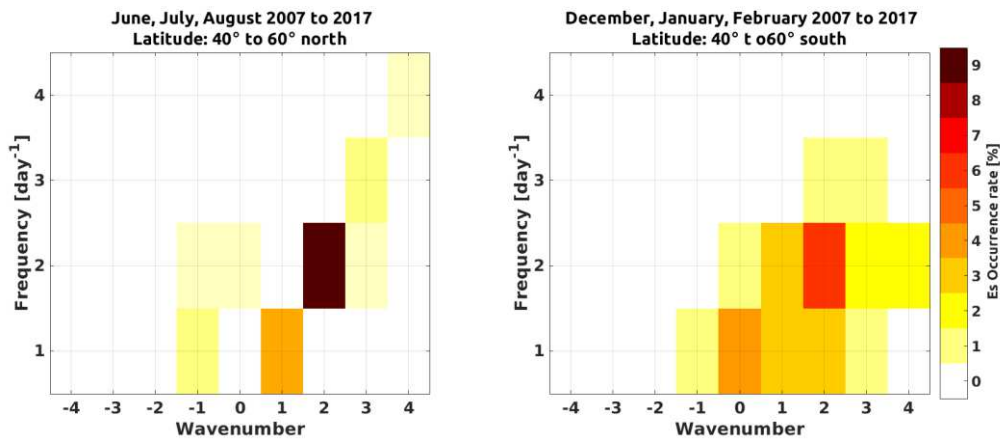


Figure 3 Solar tidal spectra of mid-latitude EsOR amplitude during northern hemisphere summer (left) and southern hemisphere summer (right)

180 The tidal spectra shown in Figure 3 correspond to the amplitude of solar tides during local
 181 summers in northern and southern midlatitudes. Different migrating and non-migrating
 182 tidal components are seen; among which the SW2 component has the highest amplitude
 183 in both summer hemispheres. For the northern hemisphere, DW1 is in second place;
 184 however, for the southern hemisphere, D0 is the second component with a high amplitude.
 185 Figure 4 shows the tidal spectra of lunar tides signature in EsOR. Unlike solar tides, lunar
 186 tidal spectra show that only SW2 component is dominant in the summer hemispheres,
 187 and other tidal components are relatively small.

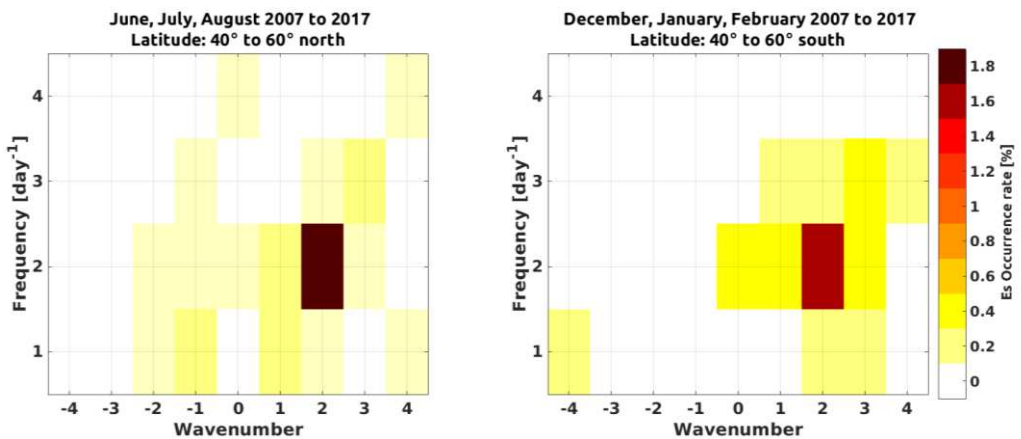


Figure 4 Lunar tidal spectra of mid-latitude EsOR during northern hemisphere summer (left) and southern hemisphere summer (right)

188 Comparison of VIC and EsOR

189 In order to compare tidal components of VIC and EsOR, tidal analysis has been
 190 performed on 11-year VIC and EsOR data sampled around 100, 105, 110, 115km altitude.

191 We studied the latitudinal variation of different tidal components of VIC and EsOR on a
 192 month-to-month basis at different altitudes. By calculating the correlation coefficients
 193 between each tidal component of VIC and EsOR at different altitudes, we realized that
 194 the altitude in which EsOR and VIC have the best correlation, vary for each component.

195 For example, Figure 5 reveals DW1 component of EsOR and VIC over different months
 196 and latitude bands at different altitudes. The seasonal variation of DW1 component of
 197 EsOR in different latitudes at 105 ± 5 km seems more similar to that of VIC at 110 and
 198 115km altitude than at 105 km. The correlation coefficient between DW1 in EsOR at

199 100±5km and VIC at 100km is 0.16, while it reaches up to 0.73 when EsOR at 105±5km

200 and VIC at 115km are taken into account. We note that in general a tidal component of

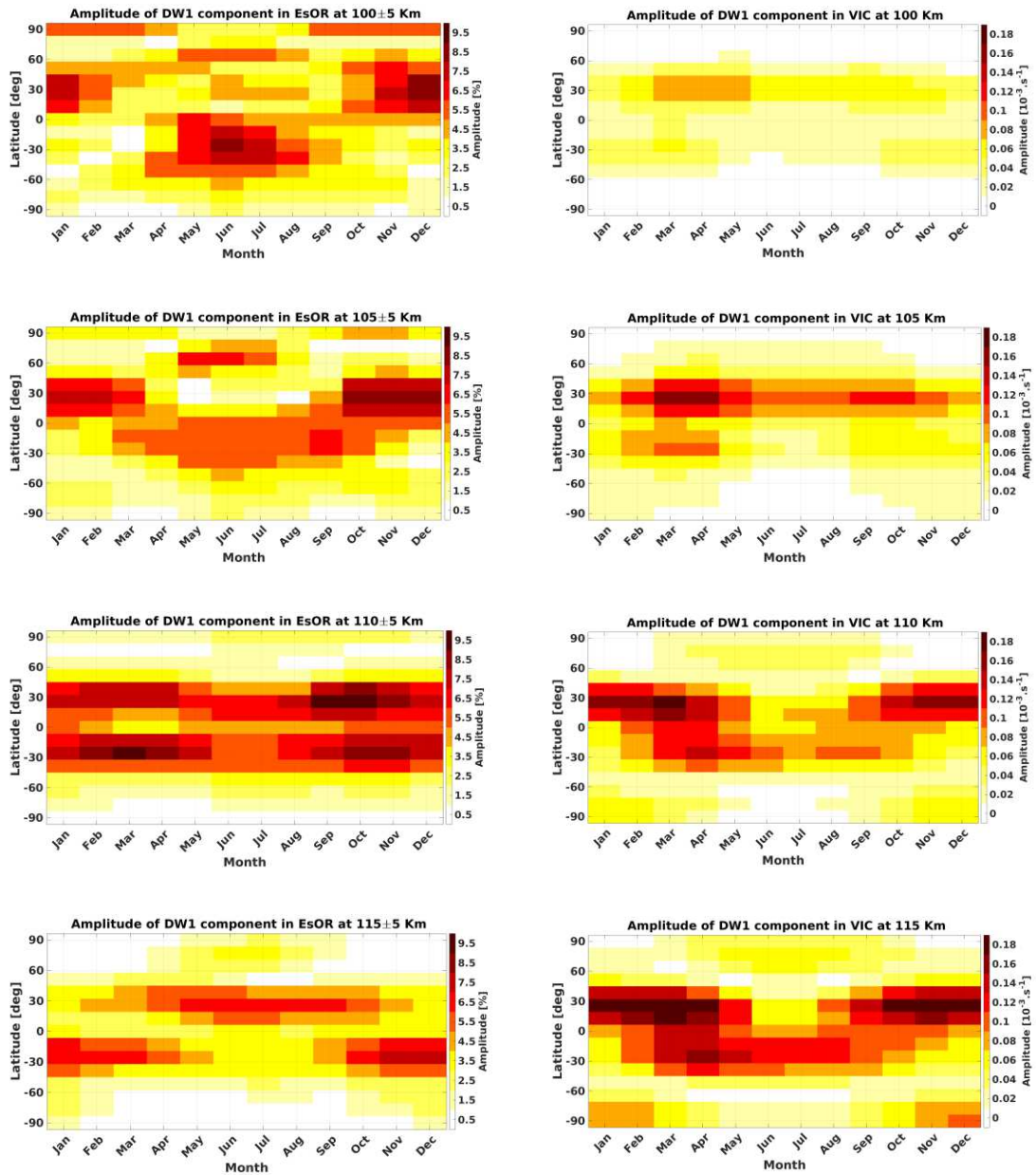


Figure 5 Month-to-month amplitude variation of DW1 component of tides in EsOR (left column) and VIC (right column) at different altitudes

201 VIC at a fixed altitude tends to correlate with the same tidal component of EsOR at a

202 higher altitude. Also the altitudes at which VIC and EsOR tidal components correlate the
203 best, differ for different tidal components. This might be due to some inaccuracies in the
204 tides of GAIA model simulations.

205 Four different migrating and non-migrating components of EsOR tidal spectra with the
206 largest amplitude were determined, and their annual variations in different latitudes are
207 displayed in Figures 6 and 7. In addition, a comparison to the corresponding VIC tidal
208 spectra at the altitude at which they have the best correlation with each other is made in
209 those figures.

210 Among all migrating components of EsOR and VIC tidal spectra, SW2 has the highest
211 amplitude. SW2 component of northern hemisphere VIC is present in all seasons, and it
212 is dominant in midlatitude local summers for EsOR and VIC. DW1 is the second,
213 regarding its amplitude which is present throughout the year around the latitude band of
214 50° south to 50° north. Subsequently, TW3 and QW4 have lower amplitudes. Although
215 month-to-month and latitudinal variations of SW2 and DW1 components of EsOR are in
216 good agreement with those in VIC, seasonal variation of QW4 in EsOR is better
217 consistent with VIC in the northern hemisphere rather than southern hemisphere; and

218 TW3 component in EsOR is not necessarily similar to that in VIC from GAIA.

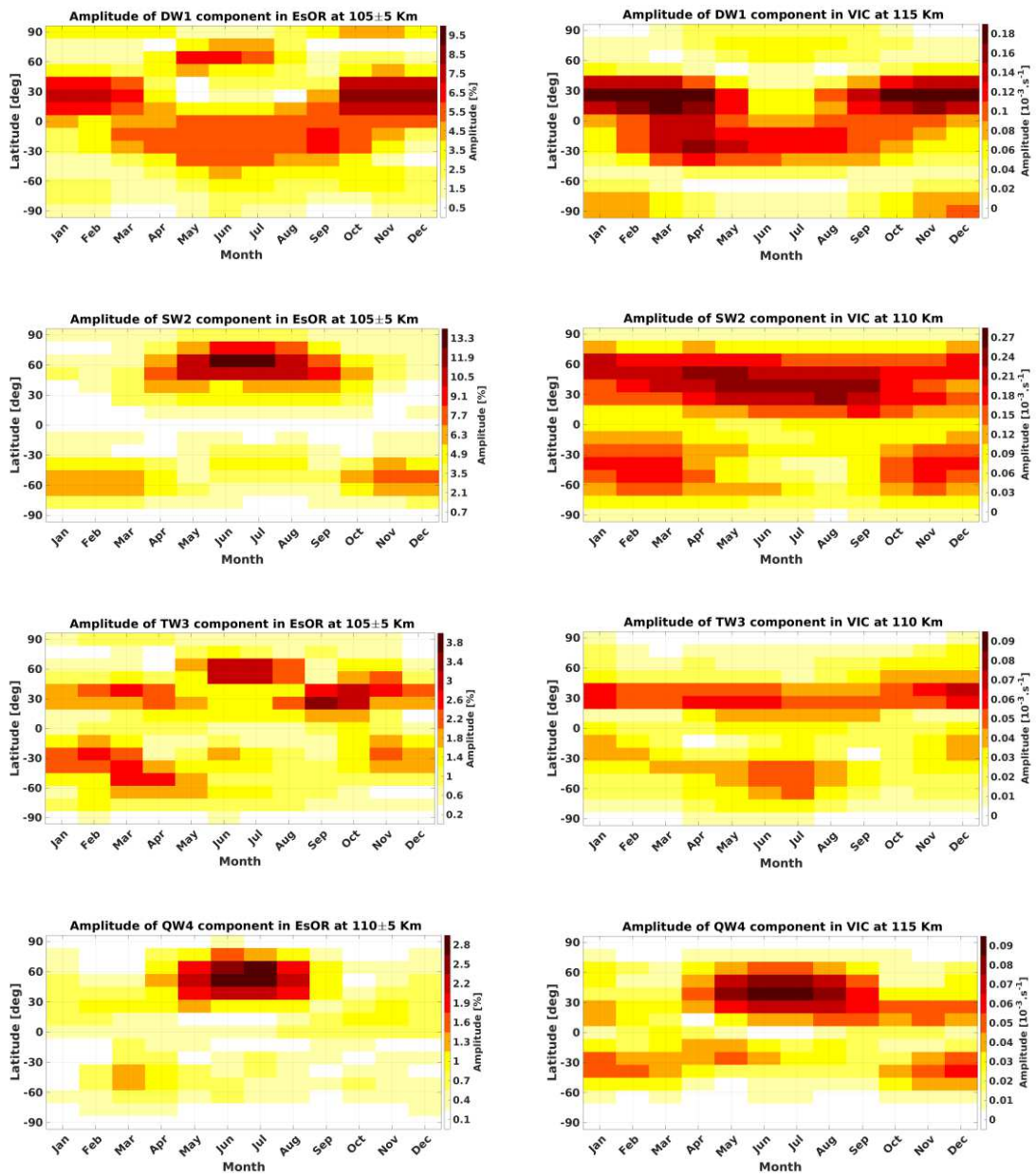


Figure 6 Month-to-month amplitude variation of migrating components of tides in EsOR (left column and right column)

219 According to Figure 7, at high and midlatitudes, SW1 has the largest amplitude among

220 all non-migrating components of EsOR and VIC. In both tidal spectra, it is dominant at

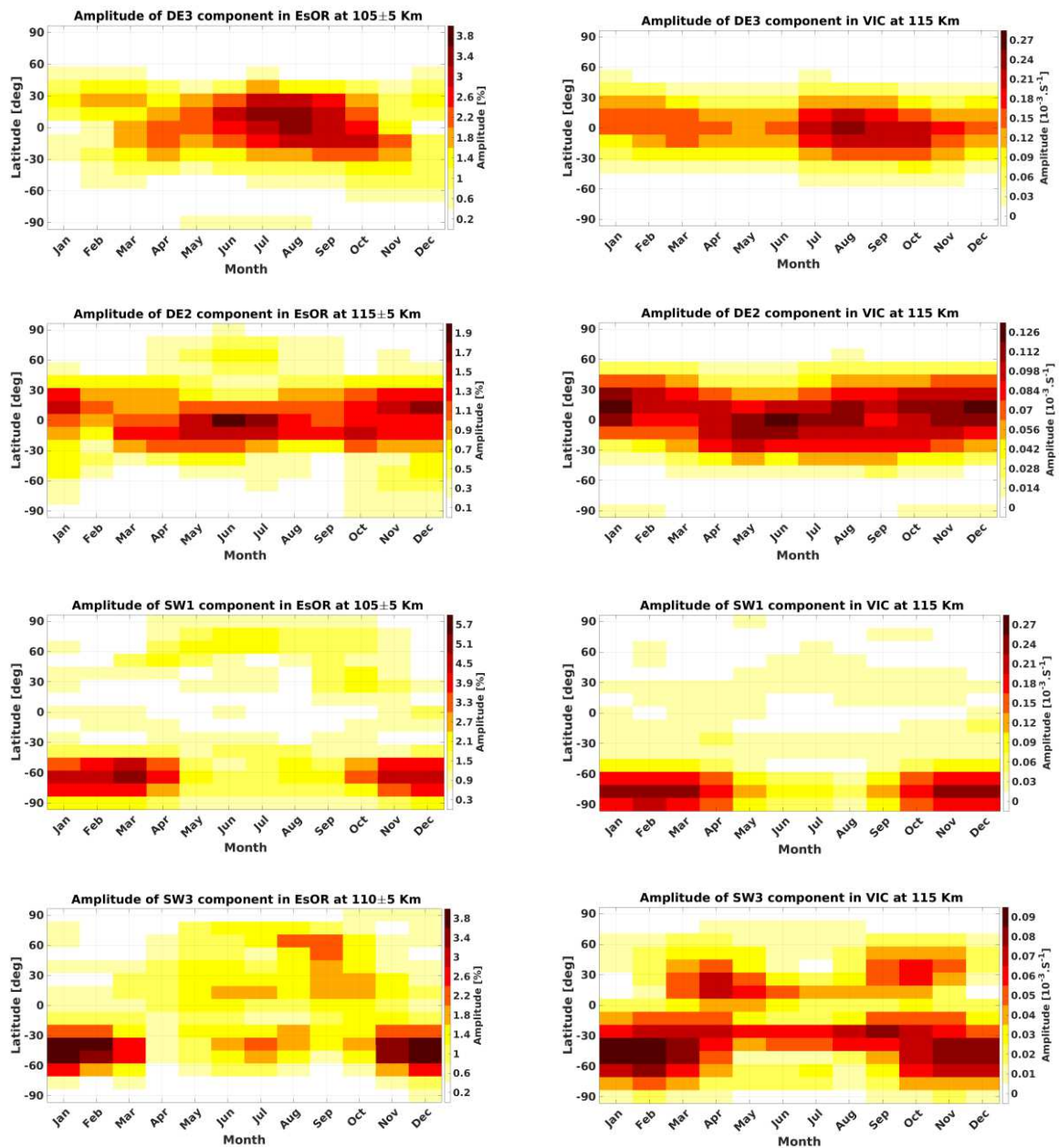


Figure 7 Month-to-month amplitude variation of non-migrating components of tides in EsOR (left column) and VIC (right column)

221 southern hemisphere high-latitude regions from November to April. The second in
 222 amplitude among non-migrating components is SW3, having similar month-to-month
 223 variation in EsOR and VIC only in the southern hemisphere.

224 At low latitudes, DE2 and DE3 have the largest amplitudes in the non-migrating
225 components of EsOR and VIC. DE3 component is dominant during July to September in
226 VIC and EsOR tidal spectra. Around winter and summer solstice in low latitudes, DE2
227 component is maximum.

228 Considering only the latitudinal variation of tidal components, DE3 of EsOR and VIC are
229 in good agreement; however, their monthly variations do not match perfectly. DE2
230 component of tides follows a similar seasonal distribution in EsOR and VIC at the latitude
231 band of 30° south to 30° north.

232 **Discussion**

233 The results have shown that tidal components in EsOR are in agreement with those in
234 VIC. In general, the consistency between tidal components in EsOR and VIC confirms
235 that wind shears generated by tides play a major role in Es layer formation.

236 According to Figure 7, SW1 and SW3 components have the highest amplitudes among
237 all non-migrating tidal components in EsOR. This can be explained by two possible
238 mechanisms. First, SW1 and SW3 in EsOR could originate from corresponding tidal
239 components in the neutral atmosphere, produced by nonlinear interaction of the SW2 and

240 stationary planetary wave with zonal wavenumber 1 in that region (Miyoshi et al., 2017).

241 Second, SW1 and SW3 in EsOR could be generated by stationary wave number 1

242 structure in is the Earth's magnetic field (\mathbf{B}) and SW2 in the horizontal neutral wind

243 velocity (\mathbf{V}), because Es layers are formed by Lorentz force ($\mathbf{V} \times \mathbf{B}$). Seasonal variations

244 of SW1 and SW3 components of VIC at different latitudes are presented in the top panel

245 of Figure 8. The middle panel shows the same, but for the zonal wind term in VIC

246 $(\partial(\frac{r \cos I}{1+r^2} \mathbf{U})/\partial z)$. The agreement of these two confirms that the vertical shear of the zonal

247 wind has the primary role in VIC. The bottom panel of Figure 8 shows the zonal wind

248 term in VIC, but magnetic field-related terms (r and I) were replaced by their zonal mean

249 to remove the effect of zonal asymmetry in the Earth's magnetic field. Comparing the two

250 bottom panels, we conclude that zonal asymmetry of the Earth's magnetic field does not

251 play a major role in the SW1 and SW3 components of VIC and consequently Es layer

252 formation. Therefore, SW1 and SW3, seen in EsOR, is due to the presence of those

253 components in the neutral atmosphere.

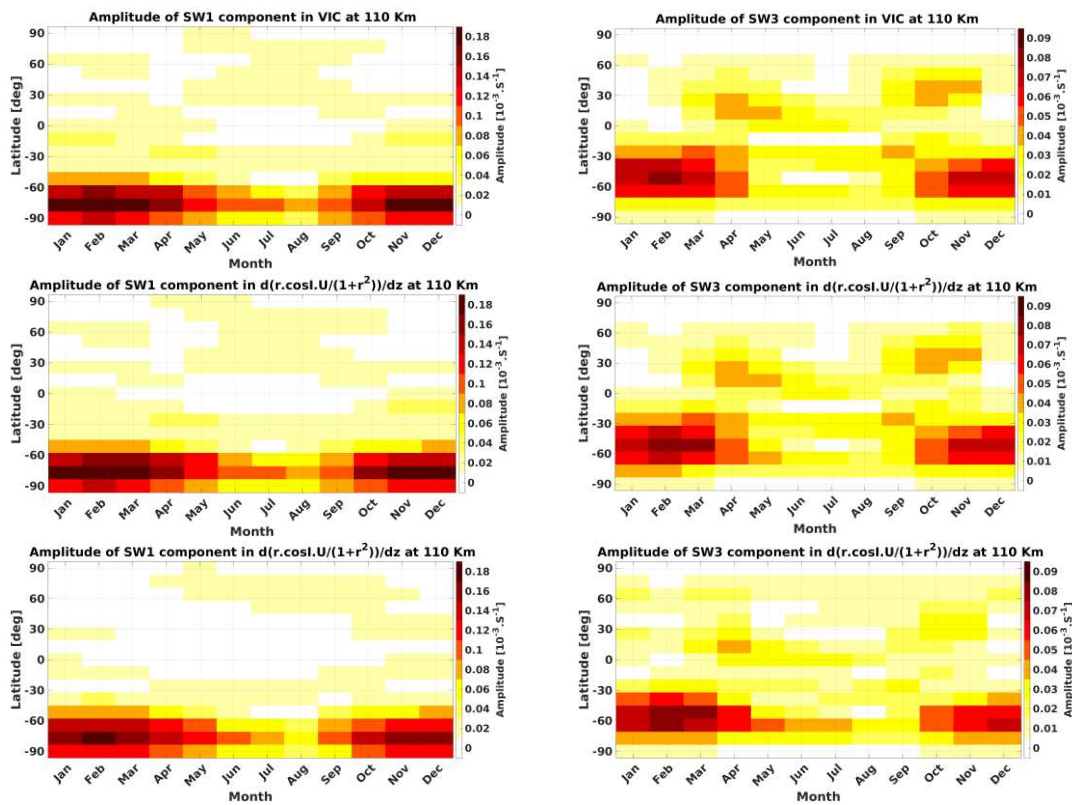


Figure 8 Month-to-month amplitude variation of SW1 (left column) and SW3 (right column) components of VIC (first row), zonal wind term in VIC (second row) and the zonal wind term VIC without the effect of magnetic field zonal asymmetry (third row) at different altitudes

254 The results of this research bring up questions that can be answered in future studies.

255 Comparison of VIC and EsOR tidal components presented in the current paper was based

256 on solar tides. Since GAIA does not include mechanisms to produce lunar tides, further

257 studies using wind models, including lunar tides, could be done to examine lunar tidal

258 components of VIC and their influence on Es layer formation. Furthermore, based on

259 Figure 5, seasonal and latitudinal variations of EsOR tidal components match those in

260 VIC at higher altitudes. Therefore, another possible future work can be performed using
261 other wind model simulations to see whether the agreement in tidal components of VIC
262 and EsOR would improve.

263 **Conclusions**

264 This study has examined the role of atmospheric tides in Es layer formation using RO
265 data of FORMASAT-3/COSMIC and GAIA model simulations. Tidal analysis has been
266 performed on EsOR and VIC to derive the amplitude of different tidal components.
267 Seasonal variations of migrating and non-migrating tidal components of EsOR and VIC
268 were also studied at different latitudes. The main results are as follows:

269 1- Analyzing 11-year Es, a semidiurnal solar and lunar tidal pattern is visible in the
270 midlatitude EsOR. This confirms previous studies (e.g., Arras et al., 2009; Matsushita,
271 1962) and provides a comprehensive picture of lunar tidal signature in Es occurrence rate,
272 using global RO data.

273 2- Performing spectral analysis on Es data, a qualitative difference between solar and
274 lunar tidal signature in EsOR is evident. Solar tides include both migrating and non-

275 migrating components, while lunar tides show only the dominance of semidiurnal
276 migrating component at midlatitude.

277 3- Deriving neutral winds from GAIA model simulation, comparisons between vertical
278 ion convergence induced by neutral winds and Es occurrence rate are made. Among all
279 different tidal components, the amplitudes of SW2, DW1, DE2 and SW1 in EsOR show
280 seasonal and latitudinal variations similar to those in the corresponding components of
281 VIC. These agreements suggest that tidal components in EsOR are primarily associated
282 with atmospheric tides.

283 4- SW1 and SW3 are the most dominant non-migrating tidal components of EsOR in
284 southern hemisphere high latitudes. SW1 and SW3 components in EsOR are likely
285 generated by the corresponding tides in neutral atmosphere. Our numerical experiments
286 suggest that the zonal asymmetry of the Earth's Magnetic field does not play a major role
287 in producing SW1 & SW3 in EsOR.

288 **List of abbreviations**

289 GAIA: Ground-to-topside model of Atmosphere and Ionosphere for Aeronomy

290 Es: Sporadic E

291 EsOR: Es Occurrence Rate

292 VIC: Vertical Ion Convergence

293 RO: Radio Occultation

294 GPS: Global Positioning System

295 FORMOSAT-3/COSMIC: FORMOsa SATellite mission-3 / Constellation Observing

296 System for Meteorology, Ionosphere and Climate

297 **Availability of data and materials**

298 Raw data of GAIA is available at: https://gaia-web.nict.go.jp/data_e.html.

299 The level 1b atmPhs radio occultation data from the F3/C mission are available at

300 COSMIC Data Analysis and Archive Center: <https://www.cosmic.ucar.edu/what-we->

301 [do/cosmic-1/data/](https://www.cosmic.ucar.edu/what-we-do/cosmic-1/data/).

302 **Competing interests**

303 The authors declare that they have no competing interests.

304 **Authors' contributions**

305 SS did the data analysis and wrote the paper. YY discussed the results and contributed to
306 revise the paper. CA extracted the Es signatures from the SNR of the GPS signal. YM &
307 HS performed GAIA simulations and the interpretation of the GAIA results. All authors
308 read and approved the final Manuscript.

309 **Funding**

310 This work was supported in part by JSPS and DFG (grant YA-574-3-1) under the Joint
311 Research Projects LEAD with DFG (JRPs-LEAD with DFG).

312 **Acknowledgements**

313 CA acknowledges support by the DFG Priority Program DynamicEarth, SPP 1788 under
314 grant AR953/1-2.

315 **References**

316 Andoh, S., Saito, A., Shinagawa, H., & Ejiri, M. K. (2020). First simulations of day-to-
317 day variability of midlatitude sporadic E layer structures. *Earth, Planets and Space*, 72(1),
318 1-9. doi: 10.1186/s40623-020-01299-8.

319 Arras, C. (2010). A global survey of sporadic E layers based on GPS Radio occultations
320 by CHAMP, GRACE and FORMOSAT-3/COSMIC (Doctoral dissertation, Deutsches
321 GeoForschungsZentrum GFZ Potsdam). doi: 10.2312/GFZ.b103-10097.

322 Arras, C., Jacobi, C., & Wickert, J. (2009, June). Semidiurnal tidal signature in sporadic
323 E occurrence rates derived from GPS radio occultation measurements at higher
324 midlatitudes. In *Annales geophysicae* (Vol. 27, No. 6, pp. 2555-2563). Copernicus
325 GmbH. doi: 10.5194/angeo-27-2555-2009.

326 Arras, C., Jacobi, C., Wickert, J., Heise, S., & Schmidt, T. (2010). Sporadic E signatures
327 revealed from multi-satellite radio occultation measurements. *Advances in Radio*
328 *Science*, 8(GHJ. 1-1/1-), 225-230. doi: 10.5194/ars-8-225-2010.

329 Arras, C., & Wickert, J. (2018). Estimation of ionospheric sporadic E intensities from
330 GPS radio occultation measurements. *Journal of Atmospheric and Solar-Terrestrial*
331 *Physics*, 171, 60-63. doi: 10.1016/j.jastp.2017.08.006.

332 Arras, C., Wickert, J., Beyerle, G., Heise, S., Schmidt, T., & Jacobi, C. (2008). A global
333 climatology of ionospheric irregularities derived from GPS radio
334 occultation. *Geophysical research letters*, 35(14). doi: 10.1029/2008GL034158.

335 Axford, W., & Cunnold, D. (1966). The wind-shear theory of temperate zone sporadic
336 E. *Radio Science*, 1(2), 191-197. doi: 10.1002/rds196612191.

337 Christakis, N., Haldoupis, C., Zhou, Q., & Meek, C. (2009, March). Seasonal variability
338 and descent of mid-latitude sporadic E layers at Arecibo. In *Annales geophysicae* (Vol.
339 27, No. 3, pp. 923-931). Copernicus GmbH. doi: 10.5194/angeo-27-923-2009.

340 Chu, Y.-H., Wang, C., Wu, K., Chen, K., Tzeng, K., Su, C.-L., Feng, W., & Plane, J.
341 (2014). Morphology of sporadic E layer retrieved from COSMIC GPS radio occultation
342 measurements: Wind shear theory examination. *Journal of Geophysical Research: Space*
343 *Physics*, 119(3), 2117-2136. doi: 10.1002/2013JA019437.

344 Finlay, C. C., Maus, S., Beggan, C., Bondar, T., Chambodut, A., Chernova, T., Chulliat,
345 A., Golovkov, V., Hamilton, B., & Hamoudi, M. (2010). International geomagnetic
346 reference field: the eleventh generation. *Geophysical Journal International*, 183(3), 1216-
347 1230. doi: 10.1111/j.1365-246X.2010.04804.x.

348 Forbes, J., Zhang, X., Palo, S., Russell, J., Mertens, C., & Mlynczak, M. (2008). Tidal
349 variability in the ionospheric dynamo region. *Journal of Geophysical Research: Space*
350 *Physics*, 113(A2). doi: 10.1029/2007JA012737.

351 Fytterer, T., Arras, C., Hoffmann, P., & Jacobi, C. (2014). Global distribution of the
352 migrating terdiurnal tide seen in sporadic E occurrence frequencies obtained from GPS
353 radio occultations. *Earth, Planets and Space*, 66(1), 1-9. doi: 10.1186/1880-5981-66-79.

354 Fytterer, T., Arras, C., & Jacobi, C. (2013). Terdiurnal signatures in sporadic E layers at
355 midlatitudes. *Advances in Radio Science*, 11(YSA), 333-339. doi: 10.5194/ars-11-333-
356 2013.

357 Haldoupis, C. (2011). A tutorial review on sporadic E layers. In: *Aeronomy of the Earth's*
358 *Atmosphere and Ionosphere*, 381-394.

359 Haldoupis, C. (2012). Midlatitude sporadic E. A typical paradigm of atmosphere-
360 ionosphere coupling. *Space Science Reviews*, 168(1), 441-461. doi: 10.1007/s11214-
361 011-9786-8.

362 Haldoupis, C., & Pancheva, D. (2002). Planetary waves and midlatitude sporadic E
363 layers: Strong experimental evidence for a close relationship. *Journal of Geophysical*
364 *Research: Space Physics*, 107(A6), SIA 3-1-SIA 3-6. doi: 10.1029/2001JA000212.

365 Haldoupis, C., & Pancheva, D. (2006). Terdiurnal tide-like variability in sporadic E
366 layers. *Journal of Geophysical Research: Space Physics*, 111(A7). doi:
367 10.1029/2005JA011522.

368 Haldoupis, C., Pancheva, D., & Mitchell, N. (2004). A study of tidal and planetary wave
369 periodicities present in midlatitude sporadic E layers. *Journal of Geophysical Research:*
370 *Space Physics*, 109(A2). doi: 10.1029/2003JA010253.

371 Haldoupis, C., Pancheva, D., Singer, W., Meek, C., & MacDougall, J. (2007). An
372 explanation for the seasonal dependence of midlatitude sporadic E layers. *Journal of*
373 *Geophysical Research: Space Physics*, 112(A6). doi: 10.1029/2007JA012322.

374 Igarashi, K., Nakamura, M., Wilkinson, P., Wu, J., Pavelyev, A., & Wickert, J. (2001).
375 Global sounding of sporadic E layers by the GPS/MET radio occultation
376 experiment. *Journal of Atmospheric and Solar-Terrestrial Physics*, 63(18), 1973-
377 1980. doi: 10.1016/S1364-6826(01)00063-3.

378 Jacobi, C., Arras, C., Geißler, C., & Lilienthal, F. (2019, May). Quarterdiurnal signature
379 in sporadic E occurrence rates and comparison with neutral wind shear. In *Annales*
380 *Geophysicae* (Vol. 37, No. 3, pp. 273-288). Copernicus GmbH. doi: 10.5194/angeo-37-
381 273-2019.

382 Jin, H., Miyoshi, Y., Fujiwara, H., Shinagawa, H., Terada, K., Terada, N., Ishii, M.,
383 Otsuka, Y., & Saito, A. (2011). Vertical connection from the tropospheric activities to the
384 ionospheric longitudinal structure simulated by a new Earth's whole atmosphere-
385 ionosphere coupled model. *Journal of Geophysical Research: Space*
386 *Physics*, 116(A1). doi: 10.1029/2010JA015925.

387 Liu, Y., Zhou, C., Tang, Q., Li, Z., Song, Y., Qing, H., Ni, B., & Zhao, Z. (2018). The
388 seasonal distribution of sporadic E layers observed from radio occultation measurements

389 and its relation with wind shear measured by TIMED/TIDI. *Advances in Space*
390 *Research*, 62(2), 426-439. doi: 10.1016/j.asr.2018.04.026.

391 Liu, Z., Fang, H., Yue, X., & Lyu, H. (2021). Wavenumber-4 Patterns of the Sporadic E
392 Over the Middle-and Low-Latitudes. *Journal of Geophysical Research: Space*
393 *Physics*, 126(8), e2021JA029238. doi: 10.1029/2021JA029238.

394 Lühr, H., & Manoj, C. (2013, August). The complete spectrum of the equatorial electrojet
395 related to solar tides: CHAMP observations. In *Annales Geophysicae* (Vol. 31, No. 8, pp.
396 1315-1331). Copernicus GmbH. Doi: 10.5194/angeo-31-1315-2013.

397 Macleod, M. A. (1966). Sporadic E theory. I. Collision-geomagnetic equilibrium. *Journal*
398 *of Atmospheric Sciences*, 23(1), 96-109. doi: 10.1175/1520-0469(1966)023.

399 Mathews, J. (1998). Sporadic E: current views and recent progress. *Journal of*
400 *Atmospheric and Solar-Terrestrial Physics*, 60(4), 413-435. doi: 10.1016/S1364-
401 6826(97)00043-6.

402 Mathews, J. D., & Bekeny, F. (1979). Upper atmosphere tides and the vertical motion of
403 ionospheric sporadic layers at Arecibo. *Journal of Geophysical Research: Space*
404 *Physics*, 84(A6), 2743-2750. doi: 10.1029/JA084iA06p02743.

405 Matsushita, S. (1952). Semidiurnal lunar variations in the sporadic-E. Journal of
406 geomagnetism and geoelectricity, 4(1), 39-40. doi: 10.5636/jgg.4.39.

407 Matsushita, S. (1957). Lunar effects on the equatorial Es. Journal of Atmospheric and
408 Terrestrial Physics, 10(3), 163-165. doi: 10.1016/0021-9169(57)90097-1.

409 Matsushita, S. (1962). Lunar tidal variations of sporadic E. In Ionospheric Sporadic (pp.
410 194-214). Elsevier. doi: 10.1016/B978-0-08-009744-2.50021-7.

411 Matsushita, S. (1967). Lunar tides in the ionosphere. In Geophysik III/Geophysics III (pp.
412 547-602). Springer, Berlin, Heidelberg. doi: 10.1007/978-3-642-46082-1_2.

413 Miyoshi, Y., Pancheva, D., Mukhtarov, P., Jin, H., Fujiwara, H., & Shinagawa, H. (2017).
414 Excitation mechanism of non-migrating tides. Journal of Atmospheric and Solar-
415 Terrestrial Physics, 156, 24-36. doi: 10.1016/j.jastp.2017.02.012.

416 Oikonomou, C., Haralambous, H., Haldoupis, C., & Meek, C. (2014). Sporadic E tidal
417 variabilities and characteristics observed with the Cyprus Digisonde. Journal of
418 Atmospheric and Solar-Terrestrial Physics, 119, 173-183. doi:
419 10.1016/j.jastp.2014.07.014.

420 Qiu, L., Zuo, X., Yu, T., Sun, Y., & Qi, Y. (2019). Comparison of global morphologies
421 of vertical ion convergence and sporadic E occurrence rate. *Advances in Space*
422 *Research*, 63(11), 3606-3611. doi: 10.1016/j.asr.2019.02.024.

423 Pancheva, D., Haldoupis, C., Meek, C., Manson, A., & Mitchell, N. (2003). Evidence of
424 a role for modulated atmospheric tides in the dependence of sporadic E layers on
425 planetary waves. *Journal of Geophysical Research: Space Physics*, 108(A5). doi:
426 10.1029/2002JA009788.

427 Richmond, A. D. (2017). Ionospheric electrodynamics. In *Handbook of Atmospheric*
428 *Electrodynamics, Volume II* (pp. 249-290). CRC Press.

429 Shinagawa, H., Miyoshi, Y., Jin, H., & Fujiwara, H. (2017). Global distribution of neutral
430 wind shear associated with sporadic E layers derived from GAIA. *Journal of Geophysical*
431 *Research: Space Physics*, 122(4), 4450-4465. doi: 10.1002/2016JA023778.

432 Stening, R. J. (1999, September). The lunar tide in sporadic E. In *Annales*
433 *Geophysicae* (Vol. 17, No. 10, pp. 1344-1351). Springer-Verlag. doi: 10.1007/s00585-
434 999-1344-2.

435 Tarpley, J., & Matsushita, S. (1971). The lunar tide in *fbEs*. *Radio Science*, 6(2), 191-
436 196. doi: 10.1029/RS006i002p00191.

437 Tarpley, J., & Matsushita, S. (1972). Lunar influences on sporadic E. *Radio Science*, 7(3),
438 411-416. doi: 10.1029/RS007i003p00411.

439 Voiculescu, M., Haldoupis, C., & Schlegel, K. (1999). Evidence for planetary wave
440 effects on midlatitude backscatter and sporadic E layer occurrence. *Geophysical research*
441 *letters*, 26(8), 1105-1108. doi: 10.1029/1999GL900172.

442 Whitehead, J. (1961). The formation of the sporadic-E layer in the temperate
443 zones. *Journal of Atmospheric and Terrestrial Physics*, 20(1), 49-58. doi: 10.1016/0021-
444 9169(61)90097-6.

445 Whitehead, J. (1970). Production and prediction of sporadic E. *Reviews of*
446 *Geophysics*, 8(1), 65-144. doi: 10.1029/RG008i001p00065.

447 Whitehead, J. (1989). Recent work on midlatitude and equatorial sporadic-E. *Journal of*
448 *Atmospheric and Terrestrial Physics*, 51(5), 401-424. doi: 10.1016/0021-
449 9169(89)90122-0.

450 Wu, D. L., Ao, C. O., Hajj, G. A., de La Torre Juarez, M., & Mannucci, A. J. (2005).
451 Sporadic E morphology from GPS-CHAMP radio occultation. *Journal of Geophysical*
452 *Research: Space Physics*, 110(A1). doi: 10.1029/2004JA010701.

453 Yeh, W. H., Liu, J. Y., Huang, C. Y., & Chen, S. P. (2014). Explanation of the sporadic-
454 E layer formation by comparing FORMOSAT-3/COSMIC data with meteor and wind
455 shear information. *Journal of Geophysical Research: Atmospheres*, 119(8), 4568-4579.
456 doi: 10.1002/2013JD020798.

Supplementary Files

This is a list of supplementary files associated with this preprint. Click to download.

- [EPSgraphic.png](#)